

Phase Diagram and Calorimetric Properties of $\text{NaFe}_{1-x}\text{Co}_x\text{As}$

A. F. Wang, X. G. Luo, Y. J. Yan, J. J. Ying, Z. J. Xiang, G. J. Ye, P. Cheng, Z. Y. Li, W. J. Hu and X. H. Chen^{1,*}

¹*Hefei National Laboratory for Physical Science at Microscale and Department of Physics, University of Science and Technology of China, Hefei, Anhui 230026, People's Republic of China*

We measured the resistivity and magnetic susceptibility to map out the phase diagram of single crystalline $\text{NaFe}_{1-x}\text{Co}_x\text{As}$. Replacement of Fe by Co suppresses both the structural and magnetic transition, while enhances the superconducting transition temperature (T_c) and superconducting component fraction. Magnetic susceptibility exhibits temperature-linear dependence in the high temperatures up to 500 K for all the superconducting samples, but such behavior suddenly breaks down for the non-superconducting overdoped crystal, suggesting that the superconductivity is closely related to the T-linear dependence of susceptibility. Analysis on the superconducting-state specific heat for the optimally doped crystal provides strong evidence for a two-band s-wave order parameter with gap amplitudes of $\Delta_1(0)/k_B T_c = 1.78$ and $\Delta_2(0)/k_B T_c = 3.11$, being consistent with the nodeless gap symmetry revealed by angle-resolved photoemission spectroscopy experiment.

PACS numbers: 74.70.Xa, 74.25.Dw, 74.25.Bt, 74.20.Rp

I. INTRODUCTION

Superconductivity in the iron-based superconductors, just like that in cuprates, emerges in the proximity to magnetically ordered state, so that the magnetic interactions are considered to play a key role in the mechanism of such high- T_c superconductivity. Accordingly, one of central issues for the iron-based superconductors is whether SDW follows a local moment or a Fermi surface nesting picture because this is correlated to the nature of the pairing force responsible for the superconductivity.¹⁻⁴ The interplay between magnetism and superconductivity has been extensively investigated in doped AeFe_2As_2 ($\text{Ae} = \text{Ca}, \text{Sr}, \text{Ba}, \text{Eu}$, and K , so called "122") family due to easiness of obtaining sizeable and high-quality single crystals.⁵ Phase diagram, through measurements of electrical transport, magnetism (susceptibility, μSR , Neutron scattering, NMR), crystal structure and so on, has been well studied in such 122 single crystals.⁶⁻¹² While for the doped NaFeAs system (so called "111"), studies for phase diagram were performed only on polycrystalline samples but not on single crystalline ones due to the hardness to growing high-quality single crystals and the difficulty to control the doping concentration. According to the same reason, little work has been done to elucidate the symmetry of the superconducting gap of doped NaFeAs system,¹³⁻¹⁵ although quite a few studies have been carried out to explore the superconducting gap structure in the isostructural LiFeAs by either specific heat or heat transport or ARPES.¹⁶⁻²⁰ Even for these few studies on the symmetry of the superconducting gap of doped NaFeAs , the results are inconsistent with each other. ARPES and heat transport experiments revealed nodeless gaps^{14,15} while the measurements of penetration depth suggested gaps with nodes.¹³

NaFeAs is established in Fe_2As structure with the in-

terstitial Fe replaced by Na atoms. Therefore, NaFeAs consists of a common building block, the FeAs layer, and the double layer of Na^+ sandwiched between the FeAs layers. NaFeAs is expected to be a simplified version of the structure of ReFeAsO ($\text{Re} = \text{rare earth}$, so called "1111") and "122" iron pnictides. There is no static magnetic ordering and structural transition in isostructural compound LiFeAs ^{21,22}, which shows superconductivity at 18 K. However, NaFeAs itself has a spin-density-wave (SDW) magnetism with a small magnetic moment ($0.09 \mu_B/\text{Fe}$)²³, in contrast to the larger values of magnetic moment $\sim 0.4 \mu_B/\text{Fe}$ in the La-"1111"³ and $\sim 0.9 \mu_B/\text{Fe}$ in the Ba-"122" parent compounds²⁴. Though NaFeAs shows superconductivity without purposely doping, it possesses only 10% superconducting volume fraction and long range AFM order exists in most of its volume inferred from the μSR study on the polycrystalline sample²⁵. By doping with Co on Fe site, bulk superconductivity in NaFeAs can be achieved. Systematical study on the doped NaFeAs single crystals by varying Co concentration has not been done yet. In this paper, we report the study on the phase diagram of single crystalline $\text{NaFe}_{1-x}\text{Co}_x\text{As}$ by measuring resistivity, magnetic susceptibility and specific heat. Additionally, susceptibility shows temperature-linear dependence up to 500 K for all the superconducting samples, and the deviation from high-temperature linear behavior occurs in the low temperatures, and the deviation temperature increases slightly with increasing the Co concentration. However, such behavior is suddenly changed for the non-superconducting overdoped crystal. Analysis on the specific heat of the optimally doped sample revealed a two-band s-wave order symmetry with two gaps with their sizes at $T = 0$ to be $\Delta_1(0)/k_B T_c = 1.78$ and $\Delta_2(0)/k_B T_c = 3.11$, suggesting the strong-coupling superconductivity.

*Corresponding author; Electronic address: chenxh@ustc.edu.cn

II. EXPERIMENTAL DETAILS

High-quality single crystals of $\text{NaFe}_{1-x}\text{Co}_x\text{As}$ have been grown by a NaAs flux method. NaAs was obtained by reacting the mixture of the elemental Na and As in evacuated quartz tubes at 200 °C for 10 h. Then Fe, Co and NaAs powder were carefully weighed according to the ratio of NaAs: Fe: Co=4: 1- x : x with ($x = 0$ - 0.3), and thoroughly ground. The mixtures were put into an alumina crucible and then sealed in an iron crucible under 1.5 atm of highly pure argon gas. The sealed crucibles were heated to 950 °C at a rate of 60 °C/h in the tube furnace filled with the inert atmosphere and kept at 950°C for 10 h, and then cooled slowly to 600 °C at 3°C/h to grow single crystals. The shiny crystals with typical size of $5 \times 5 \times 0.2 \text{ mm}^3$ can be easily cleaved from the melt. X-ray diffraction was performed on Smartlab-9 diffractometer (*Rikagu*) from 10° to 60° with a scanning rate of 2° per minute. The actual chemical composition of the single crystals is determined by energy dispersive X-ray spectroscopy (EDS). With changing the nominal x from 0 to 0.3, we obtained 12 batches of crystals, whose actual compositions were determined by EDS to be 0, 0.006, 0.010, 0.014, 0.017, 0.021, 0.028, 0.042, 0.047, 0.061, 0.070, 0.075 and 0.109, with standard instrument error as about 10%. Measurements of resistivity and specific heat were carried out by using the PPMS-9T (*Quantum Design*). Magnetic susceptibility was measured by using SQUID-MPMS-7T (*Quantum Design*), and a high-temperature oven was used in the SQUID-MPMS for magnetic susceptibility measurement above 400 K. In all the magnetic measurements, magnetic field was applied within ab-plane.

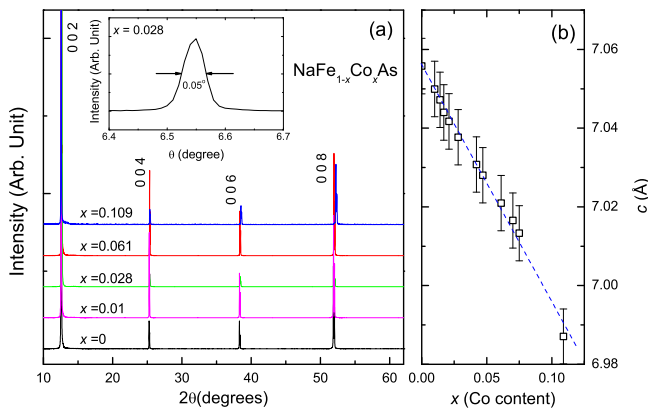


FIG. 1: (a): Selected XRD patterns for $\text{NaFe}_{1-x}\text{Co}_x\text{As}$ single crystals. (b): The lattice parameter of c -axis plotted as a function of Co concentration x . Inset in (a) is the rocking curve for the crystal with $x = 0.028$.

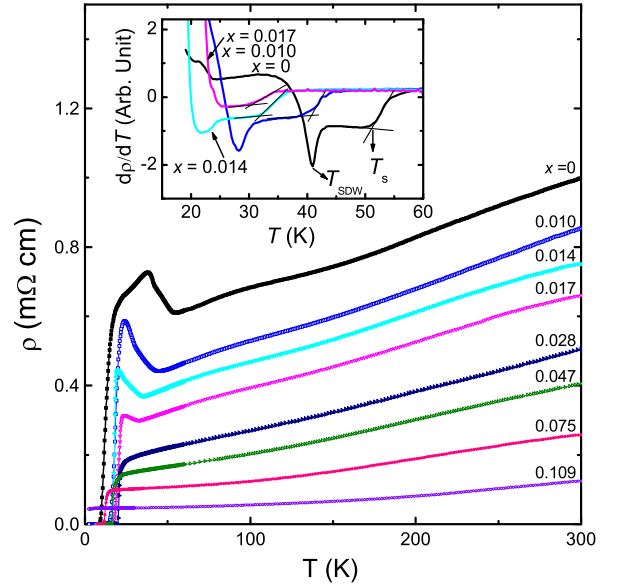


FIG. 2: Resistivity as a function of temperature for $\text{NaFe}_{1-x}\text{Co}_x\text{As}$ single crystals. Inset is the derivative resistivity for the underdoped $\text{NaFe}_{1-x}\text{Co}_x\text{As}$ single crystals, where the scenarios to determine the T_s and T_{SDW} are given.

III. RESULTS AND DISCUSSION

Figure 1(a) shows the selected single-crystalline XRD patterns for $\text{NaFe}_{1-x}\text{Co}_x\text{As}$ single crystals. Only (00 l) reflections can be recognized, and the rocking curve plotted in the inset of Fig. 1(a) shows a full-width-at-half-maximum (FWHM) about 0.05° , indicating c -axis orientation and high quality for these single crystals. Lattice parameter of c -axis (c) estimated from Fig. 1(a) was plotted as a function of Co concentration, as shown Fig. 1(b). The lattice parameter, c , of the undoped compound is 7.056 Å, being consistent with previous reported results.^{25,26} The lattice parameter decreases linearly with increasing Co doping, consistent with the results reported on polycrystalline $\text{NaFe}_{1-x}\text{Co}_x\text{As}$ samples.²⁵ While the amplitude of the change of c ($\sim 1\%$ from 0 to 0.109) is much smaller than that reported in polycrystalline samples ($\sim 4\%$).²⁵

Temperature dependence of resistivity taken from 2 to 300 K were displayed in Fig. 2 for the selected single-crystalline $\text{NaFe}_{1-x}\text{Co}_x\text{As}$ samples. The resistivity decreases with increasing Co doping level. An upturn in resistivity is observed in the low temperatures for the underdoped crystals, which arises from the structural/SDW transition. The inset shows the derivative of resistivity to figure out the temperatures corresponding to the structural and SDW transition (T_s and T_{SDW}). The two distinct features in $d\rho(T)/dT$ are used to determine the T_s and T_{SDW} . The derivative of resistivity is shown in the inset of Fig. 2. The structural and SDW transitions are suppressed rapidly with increasing Co concentration. In samples with Co concentration higher than 2.1%, no

trace of structural/SDW transition can be recognized in resistivity. The undoped compound is already superconducting although the superconducting transition is quite broad, and the resistivity of NaFeAs reaches zero at around 10 K, consistent with previous reports. The superconducting transitions for most of the samples are quite round, so we define the temperature at which resistivity reaches zero as T_c . The optimal doping level is around $x = 0.028$ and the corresponding T_c is 20 K. Further Co doping leads to the decrease of T_c , and no superconducting transition can be observed down to 2 K for the crystal with $x = 0.109$.

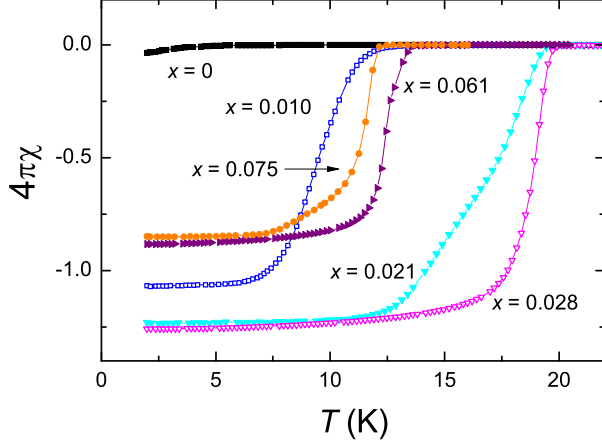


FIG. 3: Magnetic susceptibility taken at 10 Oe in ZFC mode for the superconducting samples.

Figure 3 shows the magnetic susceptibility taken at 10 Oe in zero field cooling (ZFC) procedure for the superconducting NaFe_{1-x}Co_xAs single crystals. For $x = 0$, tiny diamagnetic signal was observed below 9 K, indicating the superconductive shielding effect is weak in this composition of crystal. With enhancing Co doping level, T_c inferred from diamagnetic signal increases. The T_c determined by susceptibility is nearly the same as T_c obtained from resistivity measurements for the crystals with the same composition. The superconductive shielding fraction rises steeply with increasing Co doping level. Full shielding at 2 K can be observed for the crystal by substituting for Fe with 1% Co. The highest T_c of 20 K is obtained in the crystal with $x = 0.028$, and the superconducting transition is very steep. To our knowledge, this is the best for all the reported crystals in this system. Both shielding fraction and T_c decrease with further doping of Co.

Susceptibility up to 500 K taken under the applied magnetic field of 5 T is shown in Fig. 4(a). Because of the very close magnitude of the normal-state susceptibilities for the superconducting samples, the susceptibilities are normalized to the values at 300 K and a shift was then made for all the Co doped samples to distinguish from each other, as shown in Fig. 4(b). Rapid drops due to superconducting transition can still be observed at low temperature for the doped superconducting samples. For

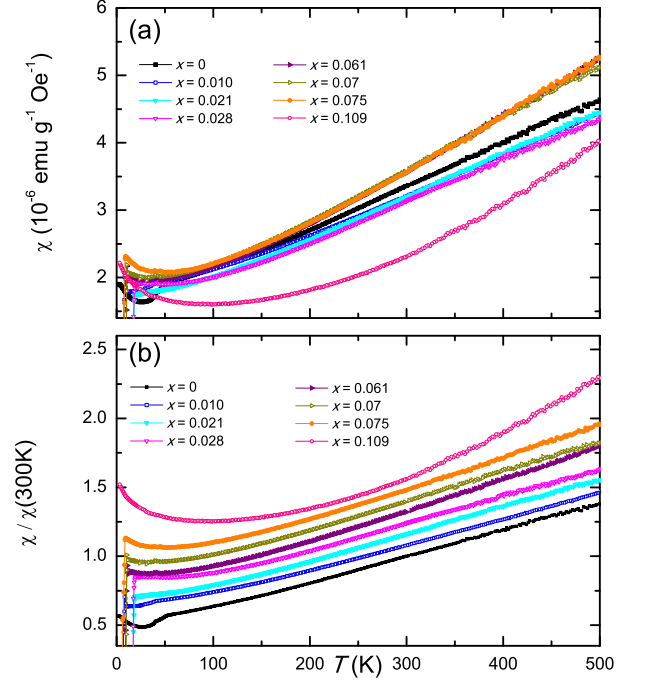


FIG. 4: (a): Normal-state susceptibility measured at 5 T in the temperature range up to 500 K for the NaFe_{1-x}Co_xAs single crystals; (b): Normalized normal-state susceptibility for the NaFe_{1-x}Co_xAs single crystals. The susceptibility was normalized to the value at 300 K and shift from sample to sample to distinguish from each other.

the undoped and underdoped samples, slight kinks can be observed in magnetic susceptibility just above T_c between 20 K and 55 K, which arises from the structural and SDW transitions. Temperature linear dependence can be observed in high temperatures for the magnetic susceptibility of all the superconducting samples. Magnetic susceptibility deviates from the high-temperature linear behavior in the low temperatures, and the deviation temperature lies at about 200 K for all the superconducting crystals. While with further increasing the Co doping level, only very weak linear behavior can be found above 400 K in heavily overdoped and non-superconducting crystal with $x = 0.109$. The slope for the linear dependence of high-temperature susceptibility is the nearly the same for all the superconducting crystals. Such temperature linear dependence of magnetic susceptibility is an universal feature for all the iron-based superconductors, which has been theoretically ascribed to the spin fluctuations arising from the local SDW correlation.²⁷ Another theoretical interpretation for the temperature linear dependence of the susceptibility is taking into account the peculiarities of orbitally resolved densities of states due to local correlations, which does not need to invoke the antiferromagnetic fluctuations.²⁸ Whether the temperature linear dependent susceptibility in high temperatures is correlated with the pairing force in the high- T_c superconductivity of the iron-based superconducting compounds is

still open question. In the present system, breakdown of the linear dependent susceptibility in the overdoped region coinciding with disappearance of superconductivity seems to suggest the association between temperature linear dependence of the susceptibility and superconductivity.

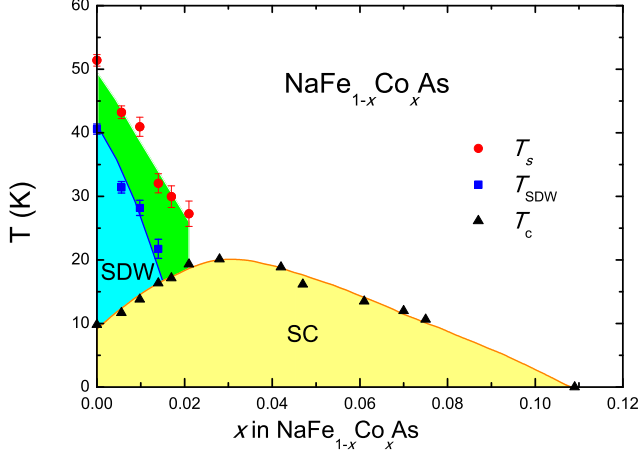


FIG. 5: Phase diagram of $\text{NaFe}_{1-x}\text{Co}_x\text{As}$. T_s , T_{SDW} and T_c are determined from the resistivity in Fig. 2 and its inset. susceptibility in Fig. 3 and Fig. 4 give almost the same value for T_s , T_{SDW} and T_c .

Based on T_s , T_{SDW} and T_c inferred from the resistivity and magnetic susceptibility, the phase diagram of $\text{NaFe}_{1-x}\text{Co}_x\text{As}$ system is established from the measurements on single crystals, as shown in Fig. 5. The gradual destruction of magnetism and enhancement of superconductivity (rise of T_c and superconductive shielding fraction) were observed with increasing Co doping level. A dome-shaped T_c vs. x relationship can be observed. Optimal T_c was obtained around $x = 0.028$ and further Co doping suppressed superconductivity. T_c goes to zero around $x = 0.109$. This phase diagram is quite similar to those of 122 and 1111 systems except for that the starting compound of the present system is superconducting. In addition, the optimal T_c can be achieved by about 2.8% Co doping in $\text{NaFe}_{1-x}\text{Co}_x\text{As}$, much less than $\sim 7\%$ Co in $\text{Ba}(\text{Fe}_{1-x}\text{Co}_x)_2\text{As}_2$ system.^{29,30} From this point of view, the phase diagram of $\text{NaFe}_{1-x}\text{Co}_x\text{As}$ is more similar to that of $\text{Ba}(\text{Fe}_{1-x}\text{Ni}_x)_2\text{As}_2$ system,³¹ in which the optimal doping is reached at 4.6%, far from that of $\sim 7\%$ in $\text{Ba}(\text{Fe}_{1-x}\text{Co}_x)_2\text{As}_2$.

Figure 6 displays the temperature dependence of the low-temperature specific heat (plotted as C_p/T) for the underdoped and heavily overdoped crystals. The specific heat for the undoped samples shown in Fig. 6(a) exhibit two anomalies corresponding to the structural and SDW transitions, respectively. The T_s and T_{SDW} are well consistent with those determined from resistivity in the inset of Fig. 2. No anomaly corresponding to the superconducting transition can be observed in the specific heat for the undoped sample, which could be due to

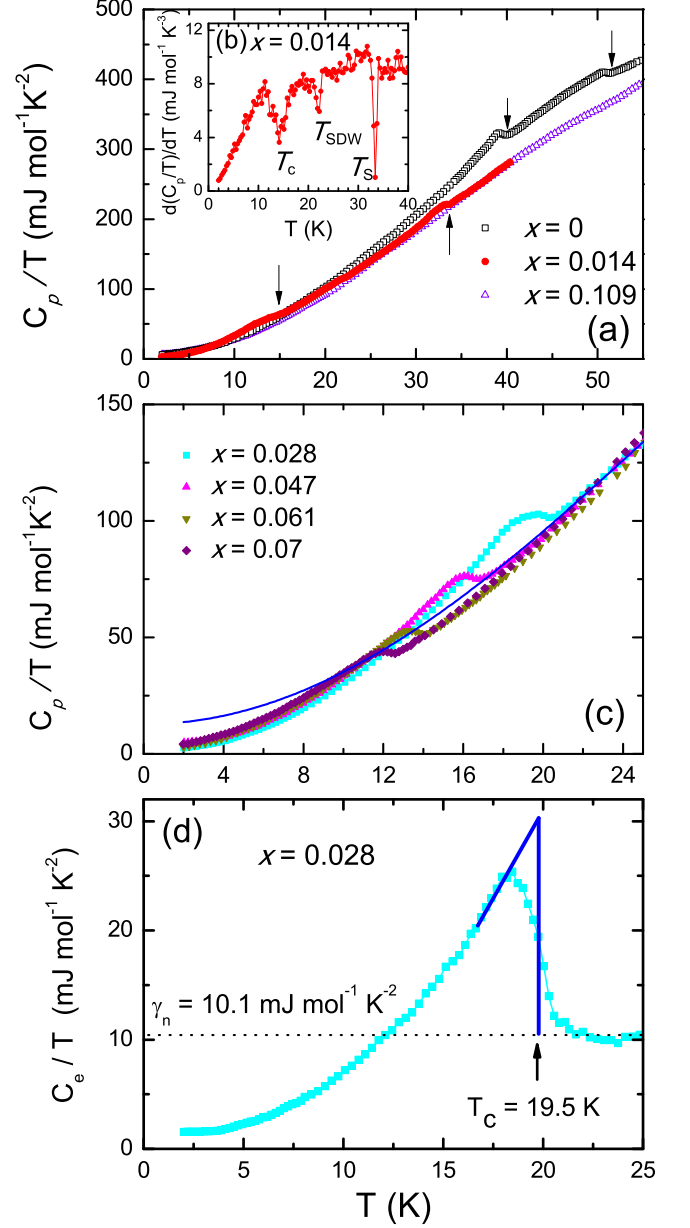


FIG. 6: (a): Temperature dependence of low-temperature specific heat (C_p/T) for underdoped and heavily overdoped $\text{NaFe}_{1-x}\text{Co}_x\text{As}$ crystals. The arrows points to the anomalies in the specific heat. (b): The inset shows the derivative of specific heat for the crystal with $x = 0.014$, where structural, SDW and superconducting transitions can be clearly recognized from the dips. (c): Specific heat as a function of temperature for the optimally-doped and overdoped superconducting $\text{NaFe}_{1-x}\text{Co}_x\text{As}$ crystals. The blue line is the fitting of the specific heat between 20 - 40 K by using $C_p = C_{\text{en}} + C_{\text{lattice}}$. (d): Electronic specific heat C_e/T (by subtracting the lattice contribution from C_p/T) as function of temperature for the optimally doped crystal, where the dashed line represents the normal-state electronic contribution, $\gamma_n = 10.1 \text{ mJ mol}^{-1} \text{ K}^{-2}$.

the low fraction of superconducting component. This is consistent with the tiny superconducting shielding fraction from susceptibility measurement shown in Fig. 3. For the crystal with $x = 0.014$, a clear anomaly corresponding to the superconducting transition around 14 K, indicating bulk superconductivity in this sample and consistent with the good superconductive shielding for crystals with $x > 0.01$ (as shown Fig. 3). In addition, an anomaly is observed at about 33 K, which coincides with the structural transition determined by the derivative of resistivity shown in the inset of Fig. 2. However, no clear anomaly corresponding to SDW transition is observed. In order to distinguish from the structural, SDW and superconducting transitions, the derivative of specific heat is shown in Fig. 6(b), and Fig. 6(b) clearly shows three dips at T_S , T_{SDW} and T_c , indicating the coexistence of the antiferromagnetism and superconductivity for the underdoped crystal with $x=0.014$. The specific heat of the heavily overdoped and non-superconducting crystal with $x = 0.109$ does not show any anomaly. As temperature increases, the specific heat above T_s for the sample with $x = 0.014$ tends to be the same as that of the sample with $x = 0.109$.

Pronounced jump due to superconducting transition can be observed in the temperature dependence of specific heat for the optimally-doped and overdoped superconducting samples, as shown in Fig. 6(c). The normal-state specific heat, C_p , can be described by $C_p = C_{en} + C_{lattice}(T)$ with the electronic contribution of $C_{en} = \gamma_n T$ and the lattice contribution of $C_{lattice}(T) = \beta T^3 + \delta T^5$. The solid line in Fig. 6(c) is the best fit to the C_p/T above T_c (20 K - 40 K) for the optimally doped sample, yielding $\gamma_n = 10.1$ mJ/mol K⁻², $\beta = 0.23$ mJ/mol K⁻⁴ and $\delta = -0.0589$ μ J/mol K⁻⁶. After subtracting this $C_{lattice}$ component, the obtained results are shown in Fig. 6(d), for which the entropy conservation is confirmed to be satisfied. Figure 6(d) shows that C_e/T does not extrapolate to zero at $T = 0$ limit but to a finite residual normal-state-like contribution $\gamma_r = 1.5$ mJ mol⁻¹ K⁻². Finite values of γ_r are a common feature in the specific measurements of iron-based superconductors.³⁴

Normalized electron specific heat is displayed in Fig. 7, where $\gamma_{es} = C_e/T$. Figure 7(a) indicates that C_e cannot be described by a single band BCS superconductor, calculated either in the weak-coupling limit with $\alpha = \Delta(0)/k_B T_c = 1.764$ or by letting α adjustable. Especially, the fitting in weak-coupling limit shows very poor agreement with the experimental data. Figure 7(a) also shows the fitting results by using the single-band d-wave model. It is clear that such a k -dependent gap, even in strong coupling scenario (obtained $\alpha = 3.09$), cannot describe the observed data. As a result, the phenomenological two-band α model with two energy gaps was used, and the fitting results are shown in Fig. 7(b). The two-band α model results in an excellent fitting of the specific heat from $T_c/10$ to T_c , and as a consequence gives reliable gaps. This fitting is calculated as the sum of the contributions from two bands by assuming independent

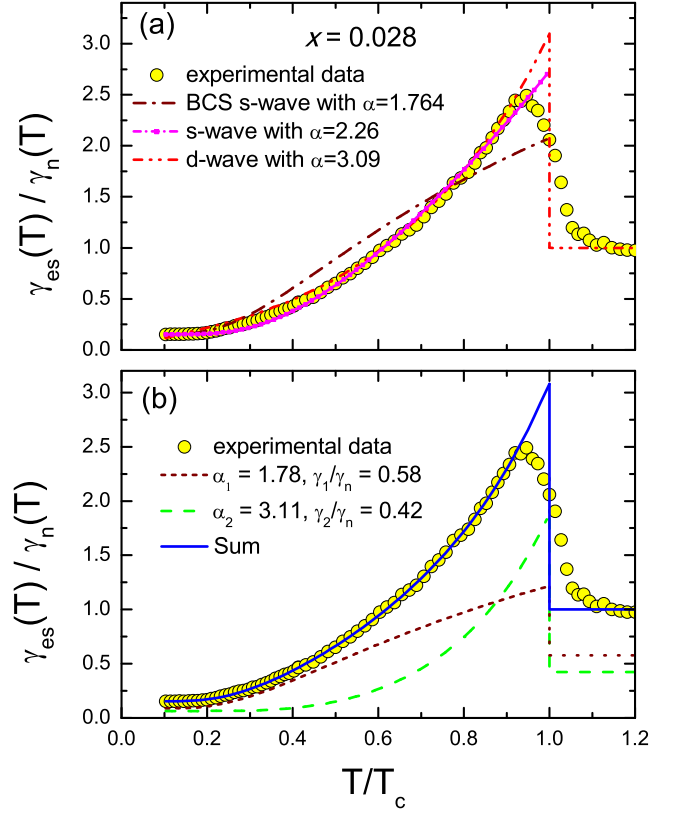


FIG. 7: (a): The normalized electron specific heat of the optimally doped crystal with $x=0.028$, compared with the specific heat of single-band s-wave (wine line) and d-wave (magenta line) order parameters as well as that in the weak-coupling limit (red line). (b): The normalized electron specific heat of the superconducting sample with $x=0.028$. The blue curve represents a two-gap fit. The wine and green curves are the partial specific-heat contributions of the two bands.

BCS temperature dependences of the two superconducting gaps, as shown by the dashed and short-dashed lines in Fig. 7(b). In the fitting, the magnitudes of two gaps at $T = 0$ limit are introduced as adjustable parameters, $\alpha_1 = \Delta_1(0)/k_B T_c$ and $\alpha_2 = \Delta_2(0)/k_B T_c$. At the same time, γ_i/γ_n ($i = 1, 2$), which measures the fraction of the total normal electron density of states, are introduced as adjustable parameters. The obtained α_1 for small gap is 1.78, and α_2 for large gap is 3.11. The relative weight for the small and large gaps here is $\gamma_1/\gamma_2 = 0.72$. Both of the obtained two gaps are larger than that of the BCS gap and one smaller in a weakly coupled two-band superconductor,³² which has been observed in MgB_2 ³³ and another iron-based superconductor $\text{Ba}(\text{Fe}_{0.925}\text{Co}_{0.075})_2\text{As}_2$ ³⁴ and as well as another 111 superconductor LiFeAs .¹⁷ Actually, such phenomenon that the two gaps are larger than the BCS weak-coupling limit has been also observed in $\text{Fe}(\text{Te}_{0.57}\text{Se}_{0.43})$ ³⁵ and $\text{Ba}_{0.6}\text{K}_{0.4}\text{Fe}_2\text{As}_2$ ³⁶ single crystals. The large mag-

nitudes of gaps derived from our fitting suggest the strong-coupling superconductivity, as that reported in $\text{Fe}(\text{Te}_{0.57}\text{Se}_{0.43})$ previously.³⁵ The relative ratio of the two gaps in $\text{NaFe}_{0.972}\text{Co}_{0.028}$ is $\Delta_1(0)/\Delta_2(0) \sim 0.57$, which is a little larger than that seen in other iron-pnictide superconductors where $\Delta_1(0)/\Delta_2(0) = 0.3 \sim 0.5$.^{34,37-39} It should be pointed out that although in the present work the fitting of specific heat suggests isotropic gaps, some theoretical and other experiments also suggest complicated pair symmetry for most of iron-based superconductors, including the nodeless anisotropic or nodal gaps. Actually, penetration depth experiment indicates a nodal gap in the optimally doped crystal,¹³ while ARPES and heat transport measurements revealed nodeless gaps in the optimally doped and overdoped $\text{NaFe}_{1-x}\text{Co}_x\text{As}$ crystal.^{14,15} Our results supports the nodeless gap symmetry observed by ARPES experiment.¹⁴ Especially, our analysis is consistent with the existence of different magnitudes of the gaps suggested by heat transport.¹⁵

IV. CONCLUSION

In summary, we mapped out the phase diagram of $\text{NaFe}_{1-x}\text{Co}_x\text{As}$ system through measuring transport and magnetic properties on high-quality single crystals. Sub-

stitution of Co for Fe destroys both the structural and magnetic transition, while enhances the superconducting transition temperature (T_c) and superconducting shielding fraction. Susceptibility exhibits temperature-linear dependence in the high temperatures up to 500 K for all the superconducting samples, while such behavior cannot be observed in the non-superconducting overdoped crystal. The breakdown of the linear dependent susceptibility in the overdoped region coinciding with disappearance of superconductivity seems to suggest the association between temperature linear dependence of the susceptibility and superconductivity. Analysis on the specific heat in superconducting state reveals a two-band s-wave order parameter with gap amplitudes of $\Delta_1(0)/k_B T_c = 1.78$ and $\Delta_2(0)/k_B T_c = 3.11$, suggesting the strong-coupling superconductivity.

Acknowledgments

This work is supported by National Natural Science Foundation of China (Grant No. 11190021, 51021091), the National Basic Research Program of China (973 Program, Grant No. 2012CB922002 and No. 2011CB00101), and Chinese Academy of Sciences.

-
- ¹ Y. Kamihara, H. Hiramatsu, M. Hirano, R. Kawamura, H. Yanagi, T. Kamiya, and H. Hosono, *J. Am. Chem. Soc.* **128**, 10012 (2006).
 - ² X. H. Chen, T. Wu, G. Wu, R. H. Liu, H. Chen, and D. F. Fang, *Nature (London)* **453**, 761 (2008).
 - ³ C. de la Cruz, Q. Huang, J. W. Lynn, Jiying Li, W. Ratcliff II, J. L. Zarestky, H. A. Mook, G. F. Chen, J. L. Luo, N. L. Wang and P. C. Dai, *Nature (London)* **453**, 899 (2008).
 - ⁴ M. Rotter, M. Tegel, and D. Johrendt, *Phys. Rev. Lett.* **101**, 107006 (2008).
 - ⁵ X. F. Wang, T. Wu, G. Wu, H. Chen, Y. L. Xie, J. J. Ying, Y. J. Yan, R. H. Liu, and X. H. Chen, *Phys. Rev. Lett.* **102**, 117005 (2009).
 - ⁶ X. F. Wang, T. Wu, G. Wu, R. H. Liu, H. Chen, Y. L. Xie, and X. H. Chen, *New J. Phys.* **11**, 045003 (2009).
 - ⁷ C. Lester, J. W. Chu, J. G. Analytis, S. C. Capelli, A. S. Erickson, C. L. Condon, M. F. Toney, I. R. Fisher, and S. M. Hayden, *Phys. Rev. B* **79**, 144523 (2009).
 - ⁸ R. W. Hu, S. L. Bud'ko, W. E. Straszheim, and P. C. Canfield, *Phys. Rev. B* **83**, 094520 (2011).
 - ⁹ M. Zhang, J. J. Ying, Y. J. Yan, A. F. Wang, X. F. Wang, Z. J. Xiang, G. J. Ye, P. Cheng, X. G. Luo, J. P. Hu, and X. H. Chen, *Phys. Rev. B* **85**, 092503 (2012).
 - ¹⁰ T. Goko et al., *Phys. Rev. B* **80**, 024508 (2009).
 - ¹¹ F. L. Ning, K. Ahilan, T. Imai, A. S. Sefat, R. Y. Jin, M. A. McGuire, B. C. Sales, and D. Mandrus, *J. Phys. Soc. Jpn.* **78**, 013711 (2009).
 - ¹² H. Chen, Y. Ren, Y. Qiu, Wei Bao, R. H. Liu, G. Wu, T. Wu, Y. L. Xie, X. F. Wang, Q. Huang, and X. H. Chen, *Europhys. Lett.* **85**, 17006 (2009).
 - ¹³ K. Cho, M. A. Tanatar, N. Spyrison, H. Kim, G. Tan, P. Dai, C. L. Zhang, R. Prozorov, arXiv: 1201.2966 (unpublished).
 - ¹⁴ Z.-H. Liu, P. Richard, K. Nakayama, G.-F. Chen, S. Dong, J.-B. He, D.-M. Wang, T.-L. Xia, K. Umezawa, T. Kawahara, S. Souma, T. Sato, T. Takahashi, T. Qian, Yaobo Huang, Nan Xu, Yingbo Shi, H. Ding, and S.-C. Wang, *Phys. Rev. B* **84**, 064519 (2011).
 - ¹⁵ S. Y. Zhou, X. C. Hong, X. Qiu, B. Y. Pan, Z. Zhang, X. L. Li, W. N. Dong, A. F. Wang, X. G. Luo, X. H. Chen, S. Y. Li, arXiv: 1204.3440 (unpublished).
 - ¹⁶ F. Wei, F. Chen, K. Sasmal, B. Lv, Z. J. Tang, Y. Y. Xue, A. M. Guloy, and C. W. Chu, *Phys. Rev. B* **81**, 134527 (2010).
 - ¹⁷ D. J. Jang, J. B. Hong, Y. S. Kwon, T. Park, K. Gofryk, F. Ronning, J. D. Thompson, Y. Bang, arXiv:1203.1362 (unpublished).
 - ¹⁸ U. Stockert, M. Abdel-Hafiez, D. V. Evtushinsky, V. B. Zabolotnyy, A. U. B. Wolter, S. Wurmehl, I. Morozov, R. Klingeler, S. V. Borisenko, B. Büchner, arXiv:1011.4246 (unpublished).
 - ¹⁹ M. A. Tanatar, J. -Ph. Reid, S. Rene De Cotret, N. Doiron-Leyraud, F. Laliberte, E. Hassinger, J. Chang, H. Kim, K. Cho, Yoo Jang Song, Yong Seung Kwon, R. Prozorov, and Louis Taillefer, *Phys. Rev. B* **84**, 054507 (2011).
 - ²⁰ D. S. Inosov, J. S. White, D. V. Evtushinsky, I. V. Morozov, A. Cameron, U. Stockert, V. B. Zabolotnyy, T. K. Kim, A. A. Kordyuk, S. V. Borisenko, E. M. Forgan, R. Klingeler, J. T. Park, S. Wurmehl, A. N. Vasiliev, G. Behr, C. D. Dewhurst, V. Hinkov, *Phys. Rev. Lett.* **104**, 187001 (2010); S. V. Borisenko, V. B. Zabolotnyy, D. V. Evtushinsky, T. K. Kim, I. V. Morozov, A. N. Yaresko, A. A. Ko-

- rdyuk, G. Behr, A. Vasiliev, R. Follath, B. Buechner, Phys. Rev. Lett. **105**, 067002 (2010).
- ²¹ X. C. Wang, Q. Q. Liu, Y. X. Lv, W. B. Gao, L. X. Yang, R. C. Yu, F. Y. Li, C. Q. Jin, Solid State Commun. **148**, 538 (2008)
 - ²² N. Qureshi, P. Steffens, Y. Drees, A. C. Komarek, D. Lamago, Y. Sidis, L. Harnagea, H. -J. Grafe, S. Wurmehl, B. Buchner, and Braden. Phys. Rev. Lett. **108**, 117001 (2012).
 - ²³ S. Li, C. de la Cruz, Q. Huang, G. F. Chen, T.-L. Xia, J. L. Luo, N. L. Wang, and P. Dai, Phys. Rev. B **80**, 020504(R) (2009).
 - ²⁴ Q. Huang, Y. Qiu, W. Bao, M. A. Green, J. W. Lynn, Y. C. Gasparovic, T. Wu, G. Wu, and X. H. Chen, Phys. Rev. Lett. **101**, 257003 (2008).
 - ²⁵ D. R. Parker, M. J. P. Smith, T. Lancaster, A. J. Steele, I. Franke, P. J. Baker, F. L. Pratt, M. J. Pitcher, S. J. Blundell, and S. J. Clarke, Phys. Rev. Lett. **104**, 057007 (2010).
 - ²⁶ Dinah R. Parker, Michael J. Pitcher, Peter J. Baker, Isabel Franke, Tom Lancaster, Stephen J. Blundell and Simon J. Clarke, Chem. Commun. **2009**, 2189C2191.
 - ²⁷ G. M. Zhang^{1(a)}, Y. H. Su², Z. Y. Lu³, Z. Y. Weng⁴, D. H. Lee⁵ and T. Xiang, Europhys. Lett. **86**, 37006 (2009)
 - ²⁸ R. Klingeler, N. Leps, I. Hellmann, A. Popa, U. Stockert, C. Hess, V. Kataev, H.-J. Grafe, F. Hammerath, G. Lang, S. Wurmehl, G. Behr, L. Harnagea, S. Singh, and B. Büchner, Phys. Rev. B **81**, 024506 (2010).
 - ²⁹ N. Ni, M. E. Tillman, J.-Q. Yan, A. Kracher, S. T. Hannahs, S. L. Bud'ko, and P. C. Canfield, Phys. Rev. B **78**, 214515 (2008).
 - ³⁰ J. H. Chu, J. G. Analytis, C. Kucharczyk, and I. R. Fisher, Phys. Rev. B **79**, 014506 (2009).
 - ³¹ N. Ni, A. Thaler, J. Q. Yan, A. Kracher, E. Colombier, S. L. Bud'ko, P. C. Canfield, and S. T. Hannahs, Phys. Rev. B **82**, 024519 (2010).
 - ³² V. Z. Kresin and S. A. Wolf, Physica C **169**, 476 (1990)
 - ³³ F. Bouquet, Y. Wang, R. A. Fisher, D. G. Hinks, J. D. Jorgensen, A. Junod, and N. E. Philips, Europhys. Lett. **56**, 567 (2001).
 - ³⁴ F. Hardy, T. Wolf, R. A. Fisher, R. Eder, P. Schweiss, P. Adelman, H. v. Löhneysen, and C. Meingast, Phys. Rev. B **81**, 060501(R) (2010).
 - ³⁵ J. Hu, T. J. Liu, B. Qian, A. Rotaru, L. Spinu, and Z. Q. Mao, Phys. Rev. B **83**, 134521 (2011).
 - ³⁶ F. Y. Wei, B. Lv, Y. Y. Xue, and C. W. Chu, Phys. Rev. B **84**, 064508 (2011).
 - ³⁷ K. Gofryk, A. S. Sefat, E. D. Bauer, M. A. McGuire, B. C. Sales, D. Mandrus, J. D. Thompson, and F. Ronning, New J. Phys. **12**, 023006 (2010).
 - ³⁸ F. Hardy, P. Burger, T. Wolf, R. A. Fisher, P. Schweiss, P. Adelman, R. Heid, R. Fromknecht, R. Eder, D. Ernst, H. v. Löhneysen, and C. Meingast, Europhys. Lett. **91**, 47008 (2010).
 - ³⁹ P. Popovich, A. V. Boris, O. V. Dolgov, A. A. Golubov, D. L. Sun, C. T. Lin, R. K. Kremer, and B. Keimer, Phys. Rev. Lett. **105**, 027003 (2010).